PCCP

PAPER

View Article Online
View Journal | View Issue

Cite this: *Phys. Chem. Chem. Phys.*, 2018, **20**, 14545

Study of oxygen evolution reaction on amorphous $Au_{13}@Ni_{120}P_{50}$ nanocluster

Yanzhou Wang,†[a] Panpan Gao,†*[a] Xiaoxu Wang,[a] Jinrong Huo,[a] Lu Li,[a]
Yajing Zhang,[a] Alex A. Volinsky,[b] Ping Qian[a] and Yanjing Su*[c]

Received 2nd February 2018,
Accepted 4th May 2018

DOI: 10.1039/c8cp00784e

rsc.li/pccp

The pursuit of catalysts to promote effective water oxidization to produce oxygen has become a research subject of high priority for water splitting. Here, first-principles calculations are employed to study the water-splitting oxygen evolution reaction (OER) on ∼1.5 nm diameter $Au_{13}@Ni_{120}P_{50}$ core–shell nanoclusters. Water splitting to produce oxygen proceeds in four intermediate reaction steps (OH*, O*, OOH* and O_2). Adsorption configurations and adsorption energies for the species involved in OER on both $Au_{13}@Ni_{120}P_{50}$ cluster and $Ni_{12}P_5(001)$ supported by Au are presented. In addition, thermodynamic free energy diagrams and kinetic potential energy changes are systematically discussed. We show that the third intermediate reaction (O* reacting with H_2O to produce OOH*) of the four elementary steps is the reaction-determining step, which accords with previous results. Also, the catalytic performance of OER for $Au_{13}@Ni_{120}P_{50}$ is better than that for $Ni_{12}P_5(001)$ supported by Au in terms of reactive overpotential (0.74 *vs.* 1.58 V) and kinetic energy barrier (2.18 *vs.* 3.17 eV). The optimal kinetic pathway for OER is further explored carefully for the $Au_{13}@Ni_{120}P_{50}$ cluster. The low thermodynamic overpotential and kinetic energy barrier make $Au_{13}@Ni_{120}P_{50}$ promising for industrial applications as a good OER electrocatalyst candidate.

1. Introduction

In the present era of increasingly exhausting fossil fuels and the associated environmental concerns, the pursuit of clean and non-polluting alternatives as energy carriers has become a research subject of high priority.[1,2] Hydrogen is regarded as an ideal candidate.[2–4] Water electrolysis to produce hydrogen is an important component of several developing clean energy technologies.[5,6] Electrochemical water splitting is composed of two half-reactions: hydrogen evolution reaction (HER) on the cathode, and oxygen evolution reaction (OER) on the anode. Water dissociation requires an applied voltage of at least 1.23 V to provide the thermodynamic driving force, and a substantially higher voltage is generally required because of the practical overpotentials associated with the reaction kinetics.[7] For instance, commercial alkaline water electrolyzers work typically at much higher voltages, from 1.8 to 2 V.[8] Water splitting always suffers from considerable energy losses.

Compared with HER, the efficiency of electrolytic hydrogen production is largely limited by OER[9,10] because the anodic reaction involves multiple proton-coupled electron transfer steps, leading to sluggish kinetics with high activation energy barriers for the O–O bond formation.[11–17] As a result, the development of cost-effective, highly active electrocatalysts for OER has become the subject of intense research in water splitting. At present, Ir- and Ru-based compounds have the highest OER activity,[18] but the high cost and scarcity of these noble metals limit the widespread adoption of water splitting. It is thus imperative to develop efficient non-noble metal electrocatalysts.

In order to design highly active catalysts from earth-abundant transition metals for OER, transition metal oxides, such as manganese oxide,[19,20] cobalt oxide[21–23] and nickel oxide,[24,25] have been widely investigated as electrode materials, exhibiting excellent electrochemical activity by synthesizing complex oxides with different structures (*e.g.* perovskite and spinel)[26–28] and various morphologies (*e.g.* nanowire and nanoparticle, *etc.*). The overpotential of these transition metal oxides, however, is still higher than that of Ir- and Ru-based catalysts. Consequently, the main challenge, to date, is to lower the substantial overpotential of earth-abundant catalysts in order to enhance the energy-harvesting efficiency.

First-row transition metal phosphide nanoparticles (NPs) are emerging as a new class of water oxidation catalysts, with reports of outstanding electrochemical catalytic performance in nickel phosphides (Ni_2P, $Ni_{12}P_5$),[29–31] cobalt phosphides (CoP)[32–35] and complex metal phosphides (CoFeP, and CoMnP).[17,36,37]

---

[a] *Department of Physics, University of Science and Technology Beijing, Beijing 100083, China. E-mail: gaopanpan@ustb.edu.cn*

[b] *Department of Mechanical Engineering, University of South Florida, Tampa, FL 33620, USA*

[c] *Advanced Material and Technology Institute, University of Science and Technology Beijing, Beijing 100083, China. E-mail: yjsu@ustb.edu.cn*

† Equally share the first authorship.

Nickel phosphides, especially, have been shown to possess naturally promising high activity, not only in HER but also in OER. Moreover, the good physical properties of nickel phosphides are also desirable for electrochemical catalytic electrodes. It is reported that nickel-rich phosphides are not only good conductors of both heat and electricity; their hardness and strength are also comparable to some ceramics.[38]

Increasing specific surface area is a favorable way to improve the efficiency of water splitting, and many efforts have been devoted to synthesizing a wide variety of nanostructures, such as NPs, nanowires, nanorods, nanotubes, and nanoplatelets. Core–shell heterogeneous nanoparticles with tunable composition and morphology exhibit multiple functionalities in catalysis. Compared with homogenous NPs, core–shell heterogeneous NPs have the following advantages. First, catalysts such as core–shell NPs allow greater tunability in reactivity and more flexibility in the nanostructure design. Second, core–shell bimetallic NPs could induce distinct strain effects to tailor catalytic reactivity and selectivity.

Density functional theory (DFT) investigations have been successfully applied to reveal the precise catalytic mechanism, involving adsorption structures, decomposition modes, reaction pathways, reaction kinetics and thermodynamics. Recently, Au@$Ni_{12}P_5$ core–shell single-crystal NPs have been experimentally shown to exhibit efficient OER catalytic ability and to be the most effective in water splitting among Au@$Ni_{12}P_5$ core–shell, Au–$Ni_{12}P_5$ oligomer-like and pure $Ni_{12}P_5$ NPs.[29] However, to the best of our knowledge, the detailed reaction of Au@$Ni_{12}P_5$ NPs in catalyzing water to generate oxygen is not convincingly accounted for at the atomic level. Herein, we modeled and developed the Au_{13}@$Ni_{120}P_{50}$ NP catalyst. Periodic DFT was performed to investigate the adsorption configurations, elementary reaction processes, potential energy surfaces and energy barrier analysis to illustrate the important role the Au_{13}@$Ni_{120}P_{50}$ nanocluster plays in OER at the anode, highlighting the crucial effect of the reaction intermediate (OOH*) on the catalytic activity. Our results indicate that oxygen formation undergoes a distinctly lower activation energy barrier with the Au_{13}@$Ni_{120}P_{50}$ NP catalyst than with the clean $Ni_{12}P_5$(001) facet.

2. Computational details and methods

All calculations in the present paper were performed by employing the Vienna ab initio simulation package (VASP)[39] based on the density functional theory (DFT) within the general gradient approximation parameterized by Perdew, Burke and Ernzerhof (PBE).[40] The electron–ion potential was described by the projector augmented wave (PAW) method[41] with 3d4s, 3s3p, and 5d6s for Ni, P and Au atoms, respectively. The plane wave expansion with kinetic cutoff of 450 eV [520 eV for the $Ni_{12}P_5$(001) slab] was used after careful convergence tests. The vacuum spaces for clusters were not less than 12 Å to avoid any artificial interactions. Energy convergence was reached when forces on the relaxed atoms were less than 0.01 eV $Å^{-1}$ in all calculations involving Au_{13}@$Ni_{120}P_{50}$ and $Ni_{12}P_5$(001) supported by bulk Au, except for the transition state locations less than 0.05 eV $Å^{-1}$ because of the high computational cost. Only the gamma point was adopted to sample the Brillouin zone for the nanocluster and adsorbed molecule, but the 3 × 3 × 1 Monkhorst–Pack grid was adopted for $Ni_{12}P_5$(001) supported by bulk Au. Smearing of 0.2 eV [0.1 eV for $Ni_{12}P_5$(001)] for the orbital occupancy was applied to achieve accurate electronic convergence in calculations involving the Au_{13}@$Ni_{120}P_{50}$ nanocluster. The ion positions were allowed to relax in order to find the minimum energy configuration using the conjugate gradient algorithm.

Simulated annealing *ab initio* molecular dynamics (AIMD) runs were carried out to obtain the ground-state core–shell structure. The Au_{13}@$Ni_{120}P_{50}$ system was initialized at 0 K and heated to 300 K over 30 ps, then cooled back down to 0 K over 90 ps. Temperature was controlled using the Nose–Hoover thermostat, and the ionic trajectories were propagated with a time step of 3 fs. Along the simulated annealing, snapshots were selected as candidates after every 2000 time steps, which were then relaxed to the nearest local minimum using the conjugate gradient algorithm. Finally, the lowest energy configuration among them was selected as the most stable core–shell structure.

For the molecule adsorption process, an empirical van der Waals (vdW) correction proposed by Grime (DFT+D3),[42] which plays an important role in weakly adsorbed systems,[43,44] was performed to describe interactions between the cluster and the adsorbates. Furthermore, the climbing image nudged elastic band (CINEB) method,[45] a tool in the VASP code, is an effective way to locate the minimum energy path from a designated initial state to a designated final state for the OER. Thus, we presented an optimized overall reactive path with the smallest potential barrier on the Au_{13}@$Ni_{120}P_{50}$ core–shell structure.

The adsorption energy (E_{ads}), which measures the strength of the interaction of the adsorbate with the cluster surface, is calculated as:

$$E_{ads} = E_{gas/cluster} - E_{gas} - E_{cluster}, \quad (1)$$

where $E_{gas/cluster}$ is the total energy of an adsorbate at the cluster, E_{gas} is the energy of the free gas-phase species and $E_{cluster}$ is the energy of the cluster. The reaction energy (ΔE) and energy barrier (E_a) of each step in the cluster were calculated according to the following formulas:

$$\Delta E = E_{FS} - E_{IS} \quad (2)$$

and

$$E_a = E_{TS} - E_{IS}, \quad (3)$$

where, E_{IS}, E_{TS} and E_{FS} are total energies of the initial state (IS), transition state (TS) and the final state (FS), respectively.

3. Results and discussion

For clarity, this section is arranged as follows. First, the structure and thermal stability of the Au_{13}@$Ni_{120}P_{50}$ nanocluster are presented. Then, the adsorption configurations of involved molecules and intermediates are discussed. Moreover, free energy diagrams, potential energy surfaces, the energy barrier and the optimal kinetic pathway are explored and analyzed.

To check the accuracy of our theoretical methods, based on the DFT combined with the GGA exchange–correlation functional, we first predicted the lattice constant, cohesive energy and the bulk modulus of $Ni_{12}P_5$ and Au at the ground-state bulk structures, respectively. Our calculated results for the ground-state structures are summarized in Table 1. Compared with the PBE, bulk properties of both $Ni_{12}P_5$ and Au based on the PBE+D3 are generally in better agreement with experiments. This is because the PBE+D3 includes both two- and three-dimensional body terms. Specifically, the PBE overestimates the lattice constants, while the equilibrium lattice constants with the PBE+D3 correction are smaller than the PBE results. Furthermore, the cohesive energy and bulk modulus computed by the PBE are generally underestimated. The results computed with the van der Waals correction (D3) are in better agreement with experiments.

3.1 Structures of Au_{13}@$Ni_{120}P_{50}$ and $Ni_{12}P_5(001)$ supported by bulk Au

Considering the practical difficulty of exploring the lowest energy configuration of the Au_{13}@$Ni_{120}P_{50}$ core–shell due to the complexity and multiple possibilities in combining the Au-core and the $Ni_{12}P_5$-shell cluster by the first-principles calculations and simulations, AIMD was employed to perform annealing-based searches for the ground-state structure in Fig. 1. Gold cluster consisting of 13 atoms was selected as a core to contribute to the core shell structure with C_{4h} due to the first magic number, according to the geometric model, to form various high symmetries. As seen in Fig. 1(a), the central atom in the Au_{13}-core cluster binds to four nearest neighboring atoms with the bond length of 2.767 Å, and a plane is formed by the five atoms, exhibiting four-fold symmetry. Each atom next to the central atom is bound to its nearest neighboring two atoms with the bond length of 2.849 Å and an angle of about 120°. Cage cylinder-like $(Ni_{12}P_5)_{10}$-cluster was constructed as a shell based on bulk $Ni_{12}P_5$ to act as the initial configuration. Stable core–shell simulated annealing nanocluster with ∼1.5 nm diameter tends to have amorphous structure, possibly attributed to multiplicity and tough tunability of the core–shell heterostructure as well as the complexity of $Ni_{12}P_5$. Considering the temperature environment in practical application, AIMD runs at 400 K were carried out to investigate thermodynamic stability using the Nose–Hoover thermostat in the canonical *NVT* ensemble. The trajectories were detected within the whole range of 6 ps simulation with step of 2 fs. The Fig. 1(b) presents the fluctuations in temperature and potential energy as a function of the simulation time. After 6 ps, structural destruction of the Au_{13}@$Ni_{120}P_{50}$ core–shell phase did not occur, except for some thermal fluctuations. The changes of bond length are small with respect to the temperature variation. It is thus reasonable to infer the thermal stability of the core–shell structure.

Table 1 Bulk properties, including lattice constants (*a*, *c*), cohesive energy (E_b) and bulk modulus (*B*) for both tetragonal $Ni_{12}P_5$ and cubic Au, calculated using PBE and PBE+D3, compared with experiments (Exp.)

	$Ni_{12}P_5$			Au		
	PBE	PBE+D3	Expt.[46]	PBE	PBE+D3	Exp.[47]
a	8.634	8.55	8.645	4.172	4.117	4.079
c (Å)	5.078	4.993	5.069	—	—	—
E_b (eV per atom)	4.93	5.44	—	2.99	3.62	3.81
B (GPa)	101.3	153.8	—	133.5	156.5	163–175

3.2 Adsorption configurations

Stable and metastable structures of species involved in OER for the Au_{13}@$Ni_{120}P_{50}$ are presented in Fig. 2 and 3, respectively. For comparison, we also studied flat and clean surfaces of $Ni_{12}P_5(001)$ due to its more stable facet compared to other facets.[48] Adsorption energy and structural parameters of adsorption configurations are listed in Table 2 for the nanocluster and in Table 3 for the $Ni_{12}P_5(001)$ supported by bulk Au. As shown in Fig. 2, the most stable adsorption configuration of H_2O was at the top site of one convex Ni atom on the Au_{13}@$Ni_{120}P_{50}$ NP surface, with the O–Ni bond length obtained with D3 being 2.023 Å and the adsorption energy of −0.831 eV. The straight line made by the oxygen atom of water molecule bonded to one nickel atom is almost perpendicular to the plane formed by the water molecule, which is in accord with the evidence[49] that O atom binds preferentially near the top site of the transition metal atoms, and the plane formed by the water molecule is nearly parallel to the surface. For isolated gas-phase water molecule, optimized O–H bond length and HOH angle are 0.972 Å and 104.5°, respectively, in excellent agreement with experimental[50] values (O–H bond lengths of 0.96 Å and HOH angle of 104.5°) obtained by spectroscopic techniques. O–H bond length of 0.975 Å and HOH angle of 106.6° were found for the water molecule adsorbed on the cluster. This indicates that the molecular structure of H_2O is slightly perturbed upon adsorption, which is crucial for the OER on the cluster.

The strongest adsorption among all possible modes for adsorbed OH is due to the oxygen atom in the OH radical located at the Ni–Ni bridge site, whose binding energy is −3.803 eV, with the O–Ni bond lengths of 1.907 Å and 1.943 Å, respectively. Compared with the free radical (0.988 Å), the bond length of OH adsorbed on the cluster (0.975 Å) is reduced by 0.013 Å, indicating that the new O–Ni bond has weakened the OH bond strength.

The most energetically favorable configuration among all possible modes of atomic oxygen binding is the oxygen at the convex Ni–P bridge site, with O–Ni binding length of 1.918 Å and O–P binding length of 1.577 Å. The corresponding optimized binding energy is −5.814 eV, which seems to indicate a stronger interaction somewhat between atomic oxygen and atomic nickel and phosphorus, which is unfavorable for the subsequent atomic oxygen reaction with adjacent molecular water to produce OOH.

H atom shows the highest preference for the Ni three-fold hollow site, with an adsorption of −2.990 eV. The H–Ni bond length ranges from 1.677 Å to 1.781 Å. The metastable structures

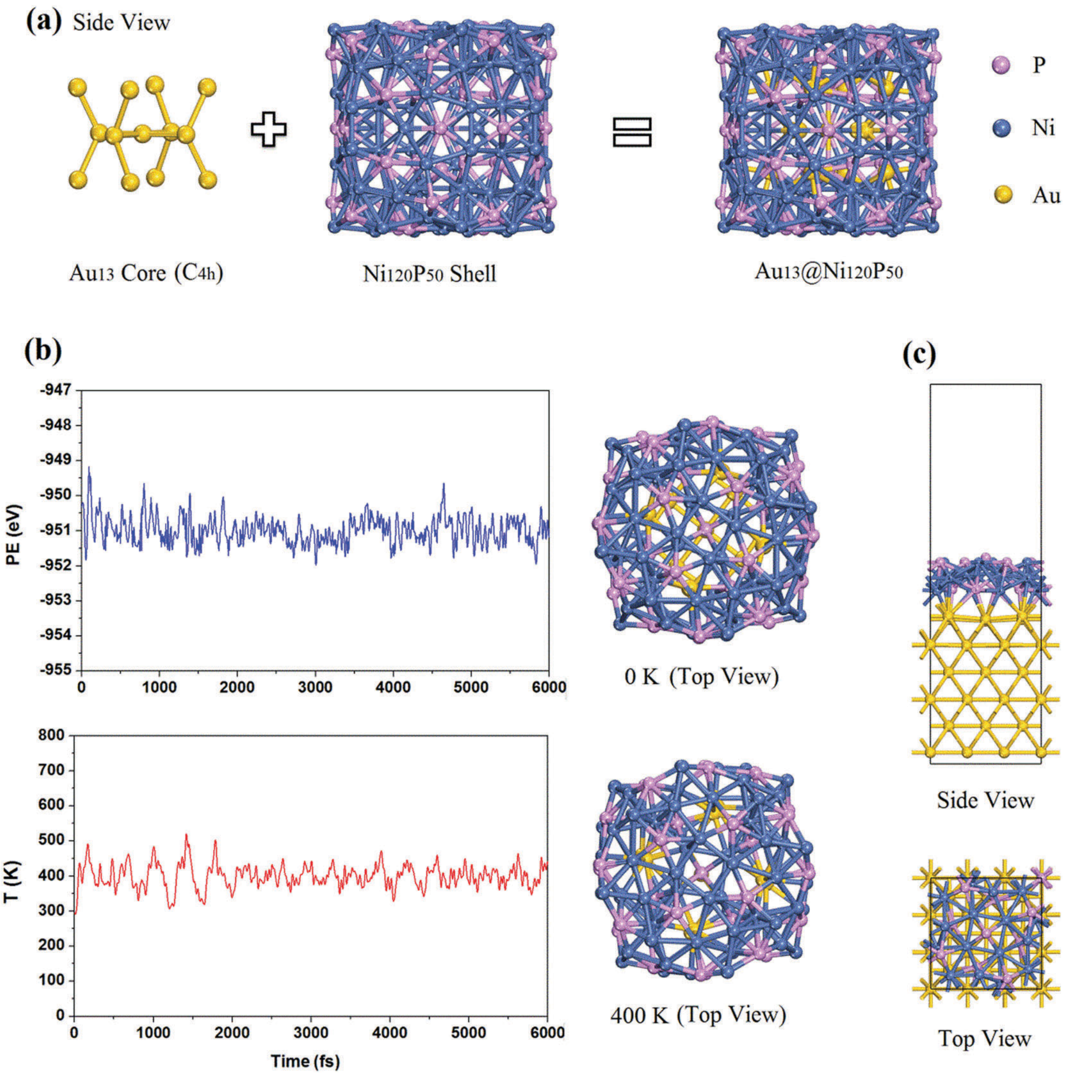

Fig. 1 (a) Optimized $Au_{13}@Ni_{120}P_{50}$ core–shell nanostructure with ∼1.5 nm diameter; (b) the fluctuations of potential energy (PE) and temperature (T) as a function of AIMD simulation time at 400 K, as well as the comparison of the core–shell structural stability between 0 K and 400 K; (c) optimized $Ni_{12}P_5$(001) supported by bulk Au. Pink balls denote P atoms; dark blue, Ni atoms; and yellow, Au atoms.

have similar binding energy, varying between −2.194 eV and −2.222 eV in spite of various adsorption configurations, such as top Ni mode, top P mode, and Ni–P bridge mode.

OOH prefers to bind to the cluster surface *via* the O^2 bridge(Ni$_v^2$) mode with the adsorption energy of −2.121 eV, in which each atom of O–O fragment sits at different Ni top sites. The adsorbed OOH has the O–O bond length of 1.553 Å, the O–H bond length is 0.983 Å, and the O–Ni bond length varies from 1.806 Å to 1.992 Å. The O–H bond length stretches by 0.008 Å compared with adsorbed OH in the O bridge(Ni$_v^2$) configuration, indicating that breaking the O–H bond in the adsorbed OOH radical is more feasible. However, that makes it easy the for the O–O bond to be ripped by Ni atoms in the hollow site compared with the O top(Ni$_v$) mode.

O_2 prefers the three-fold hollow site with the O^2 hollow(Ni$_v^3$) mode, at the adsorption energy of −1.943 eV. The O–O bond is 1.490 Å long, and the O–Ni bond changes in the 1.88–2.04 Å range. Both O atoms are bonded to the surface, favoring parallel configuration. In this configuration, the O_2 molecule binds to Ni atoms as much as possible, indicating the preference of the O atom to associate with Ni atoms on the cluster surface. Such strong adsorption configuration makes it difficult for O_2 to get rid of the bond from the catalyst to become a free molecule.

3.3 Evaluation of thermochemical potential and energy diagrams

Calculation of electrochemical barriers in aqueous environments using DFT is still quite difficult compared to thermal behavior in gas phase systems.[51] However, due to the fact that the energetics of the transition states and intermediates scale with one another, thermodynamic descriptors can be useful in predicting and explaining trends in catalytic activity.[52] We consider four elementary steps for OER, with each consisting

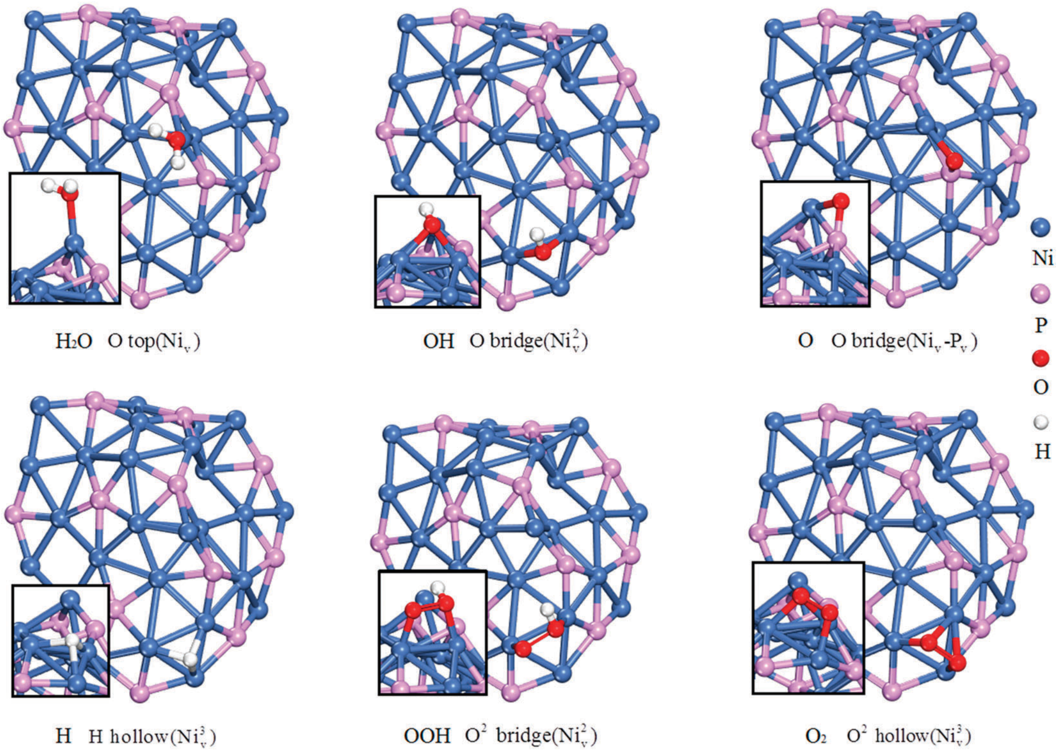

Fig. 2 Top view and side view (inset) of stable adsorption configurations with D3 correction involved in OER on the Au_{13}@$Ni_{120}P_{50}$ nanocluster surface. Blue, pink, red and white balls denote Ni, P, O and H atoms, respectively. Top, bridge and hollow represent the adsorption site; the A^X site (M^Z) descriptor denotes X atom A(s) in adsorbed species directly interacting with the Z surface atom M(s) on the core–shell cluster, and the subscripts letters v and p indicate the surface convex M atom and planar atom of the core–shell cluster, respectively.

of a single proton–electron transfer step reaction written as the following sequential equations.[52]

Step 1:

$$H_2O_{(l)} + * \xrightarrow{\Delta G_1} OH^* + H^+/e^- \quad (4)$$

Step 2:

$$OH^* \xrightarrow{\Delta G_2} O^* + H^+/e^- \quad (5)$$

Step 3:

$$O^* + H_2O_{(l)} \xrightarrow{\Delta G_3} OOH^* + H^+/e^- \quad (6)$$

Step 4:

$$OOH^* \xrightarrow{\Delta G_4} O_{2(g)} + * + H^+/e^- \quad (7)$$

Here, the asterisk denotes adsorbed surface sites, such as bridge (Ni–Ni) site, bridge (Ni–Ni) site, top (Ni or P) site, and hollow (Ni–Ni–Ni) site, *etc.* The free energy change ($\Delta G_{1\text{–}4}$) of each elementary step is described by the following expressions:[53]

$$\Delta G_1 = \Delta G_{OH^*} - \Delta G_{H_2O} - eU + k_bT\ln a_{H^+} \quad (8)$$

$$\Delta G_2 = \Delta G_{O^*} - \Delta G_{OH^*} - eU + k_bT\ln a_{H^+} \quad (9)$$

$$\Delta G_3 = \Delta G_{OOH^*} - \Delta G_{O^*} - eU + k_bT\ln a_{H^+} \quad (10)$$

$$\Delta G_4 = \Delta G_{O_2} - \Delta G_{OOH^*} - eU + k_bT\ln a_{H^+}, \quad (11)$$

where a_{H^+} represents the activity of the protons, and U represents the applied potential. Theoretical overpotential is independent of the pH or the potential values, as the free energy obtained by using eqn (8)–(11) vary in the same way with pH and U, indicating that the potential-determining step remains the same. The effect of liquid water was implicitly taken into account, as we used liquid water as a reference. Therefore, the expressions ($\Delta G_{1\text{–}4}$) for the free energy at standard conditions (pH = 0, T = 298.15 K and U = 0: $\Delta G^0_{1\text{–}4}$) were simplified by the following equations ($\Delta G^0_{1\text{–}4}$):

$$\Delta G^0_1 = \Delta G_{OH^*} \quad (12)$$

$$\Delta G^0_2 = \Delta G_{O^*} - \Delta G_{OH^*} \quad (13)$$

$$\Delta G^0_3 = \Delta G_{OOH^*} - \Delta G_{O^*} \quad (14)$$

$$\Delta G^0_4 = \Delta G_{O_2} - \Delta G_{OOH^*} \quad (15)$$

Here, $\Delta G^0_{1\text{–}4}$ is $\Delta G_{1\text{–}4}$ at U = 0 (pH = 0 and T = 298.15 K). The free energy of each adsorbate is solved using the computational standard hydrogen electrode (SHE), allowing the replacement of a proton and an electron with half a hydrogen molecule at U = 0 V *vs.* SHE by referencing liquid water and hydrogen gas at standard conditions:

$$\Delta G_{OH^*} = E^{DFT}_{OH^*} - E^{DFT}_{*} - E^{DFT}_{H_2O} + \frac{1}{2}E^{DFT}_{H_2} + \hat{G}_{OH^*} \quad (16)$$

$$\Delta G_{O^*} = E^{DFT}_{O^*} - E^{DFT}_{*} - E^{DFT}_{H_2O} + E^{DFT}_{H_2} + \hat{G}_{O^*} \quad (17)$$

$$\Delta G_{OOH^*} = E^{DFT}_{OOH^*} - E^{DFT}_{*} - 2E^{DFT}_{H_2O} + E^{DFT}_{H_2} + \hat{G}_{OOH^*} \quad (18)$$

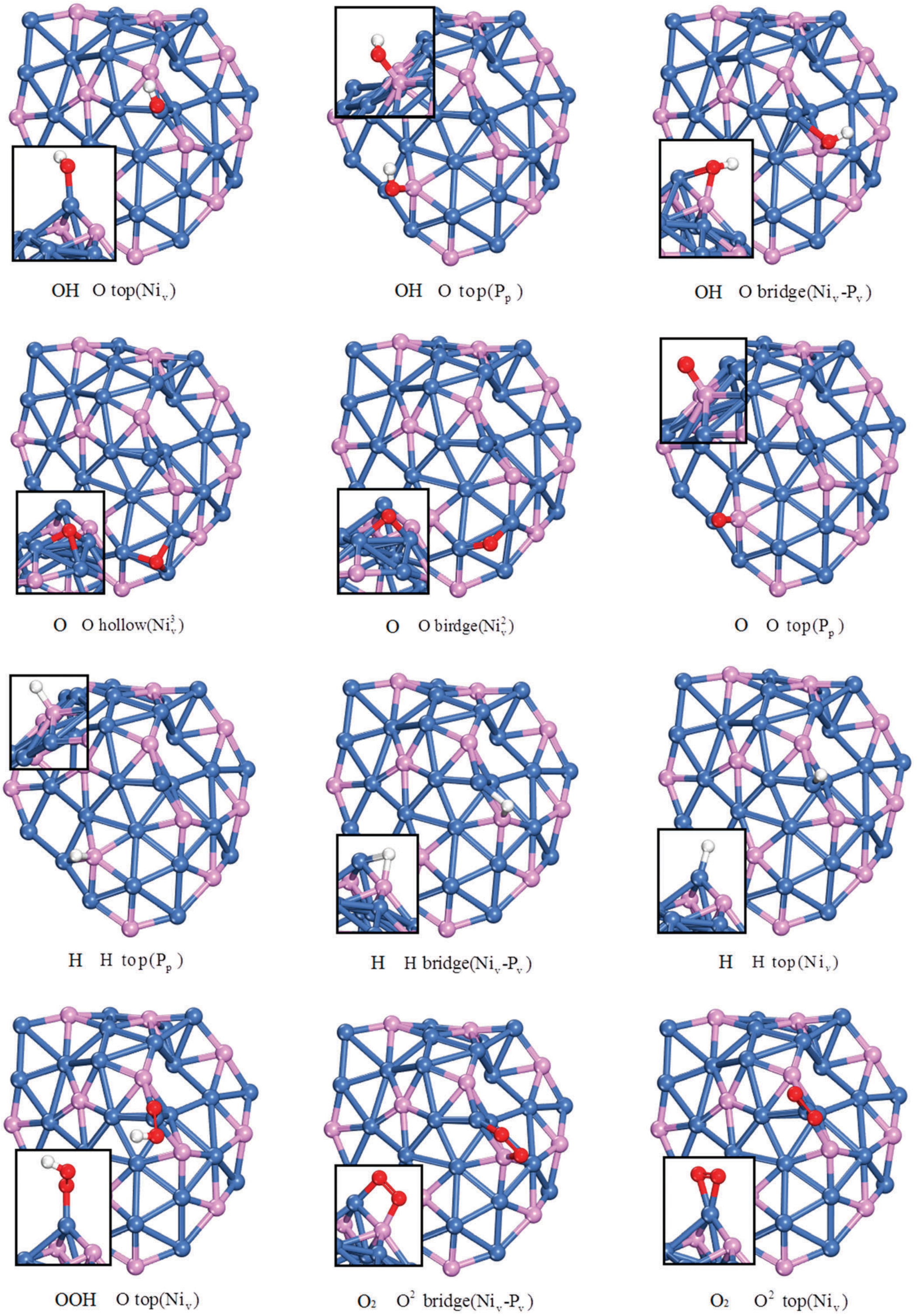

OH O top(Ni_v) OH O top(P_p) OH O bridge(Ni_v-P_v)

O O hollow(Ni_v^3) O O birdge(Ni_v^2) O O top(P_p)

H H top(P_p) H H bridge(Ni_v-P_v) H H top(Ni_v)

OOH O top(Ni_v) O_2 O^2 bridge(Ni_v-P_v) O_2 O^2 top(Ni_v)

Fig. 3 Top view and side view (inset) of the metastable adsorption configurations with D3 correction involved in the OER on the $Au_{13}@Ni_{120}P_{50}$ NP surface.

for which E_*^{DFT}, $E_{\mathrm{OH}^*}^{\mathrm{DFT}}$, $E_{\mathrm{O}^*}^{\mathrm{DFT}}$ and $E_{\mathrm{OOH}^*}^{\mathrm{DFT}}$ are the ground state energy of the clean surface and the surfaces with OH*, O*, and OOH* adsorbed, respectively. $E_{\mathrm{H_2O}}^{\mathrm{DFT}}$ and $E_{\mathrm{H_2}}^{\mathrm{DFT}}$ are the calculated energy of H_2O and H_2 molecules, respectively, in the gas phase. Here, $\hat{G}_i$ includes contributions from vibration energy and entropy of the adsorbate at 298.15 K. This correction was calculated using the harmonic approximation for every adsorbate and surface studied, with typical values of 0.35, 0.05, and 0.40 for OH*, O*, and OOH*, respectively.[52]

Table 2 Adsorption configurations, adsorption energy and structural parameters for species involved in OER on the $Au_{13}@Ni_{120}P_{50}$ NPs surface. Meaning of configuration descriptors are the same as in Fig. 2

	Configuration	PBE			PBE+D3		
Species	A^Xsite($M^Z_{v/p}$)	E_{ads}, eV	$d_{O/H–Ni/P}$, Å	$d_{O–O/H}$, Å	E_{ads}, eV	$d_{O/H–Ni/P}$, Å	$d_{O–O/H}$, Å
H_2O	O top(Ni_v)	−0.769	2.027	0.974, 0.974	−0.831	2.023	0.975, 0.975
O_2	O^2 hollow($Ni_v{}^3$)	−1.783	1.88–2.047	1.489	−1.943	1.88–2.04	1.49
	O^2 bridge(Ni_v–P_v)	−1.522	1.819, 1.656	1.511	−1.63	1.818, 1.655	1.512
	O^2 top(Ni_v)	−1.164	1.843, 1.869	1.371	−1.221	1.869, 1.842	1.372
OOH	O^2 bridge($Ni_v{}^2$)	−1.935	1.807, 1.991	1.556, 0.982	−2.121	1.806, 1.992	1.553, 0.983
	O top(Ni_v)	−1.924	1.79	1.458, 0.981	−1.972	1.794	1.464, 0.981
OH	O bridge($Ni_v{}^2$)	−3.665	1.911, 1.942	0.975	−3.803	1.907, 1.943	0.975
	O top(Ni_v)	−3.349	1.786	0.974	−3.392	1.784	0.974
	O top(P_p)	−3.236	1.662	0.978	−3.308	1.662	0.978
	O bridge(Ni_v–P_v)	−3.150	2.16, 1.753	0.979	−3.241	2.160, 1.748	0.979
O	O bridge(Ni_v–P_v)	−5.771	1.918, 1.577	—	−5.814	1.918, 1.577	—
	O hollow($Ni_v{}^3$)	−5.457	1.826–1.945	—	−5.519	1.825–1.951	—
	O bridge($Ni_v{}^2$)	−5.313	1.775, 1.762	—	−5.392	1.774, 1.76	—
	O top(P_p)	−5.146	1.514	—	−5.174	1.514	—
	O top(Ni_v)	−4.061	1.641	—	−4.084	1.641	—
H	H hollow($Ni_v{}^3$)	−2.929	1.679–1.774	—	−2.99	1.677–1.781	—
	H top(P_p)	−2.206	1.435	—	−2.198	1.434	—
	H bridge(Ni_v–P_v)	−2.198	1.754, 1.55	—	−2.222	1.749, 1.548	—
	H top(Ni_v)	−2.194	1.498	—	−2.194	1.496	—

Table 3 Most stable configurations, adsorption energy and structural parameters for species involved in OER on the $Ni_{12}P_5(001)$ supported by bulk Au

	Configuration	PBE			PBE+D3		
Species	A^Xsite(M)	E_{ads}, eV	$d_{O/H–Ni/P}$, Å	$d_{O–O/H}$, Å	E_{ads}, eV	$d_{O/H–Ni/P}$, Å	$d_{O–O/H}$, Å
H_2O	O top(Ni)	−0.581	2.199	0.976, 0.983	−0.802	2.186	0.978, 0.984
O_2	O^2 bridge(Ni–P)	−1.404	1.939, 1.640	1.48	−1.671	1.937–1.639	1.478
OOH	O top(Ni)	−1.199	1.886	1.436, 0.982	−1.394	1.88	1.432, 0.986
OH	O top(P)	−3.606	1.639	0.977	−3.749	1.637	0.977
O	O top(P)	−5.87	1.499	—	−5.996	1.499	—
H	O top(P)	−2.593	1.421	—	−2.636	1.42	—

In order to avoid the calculation of the O_2 bond energy, which is hard to obtain accurately with DFT, we instead substituted the experimental formation energy of H_2O when calculating the final step:

$$2H_2 + O_2 \rightarrow 2H_2O,\ \Delta G^0 = -4.92\ \text{eV} \tag{19}$$

Therefore,

$$\Delta G_{O_2(g)} = 4.92\ \text{eV} \tag{20}$$

A very important method has been proven to be feasible, where the catalytic performance is estimated by the magnitude of the potential-determining step for the OER. More precisely, it is the calculation of theoretical overpotential, which is the overpotential required to make all four elementary steps exergonic. Thus, the theoretical overpotential is given as:[53]

$$\eta = \max(\Delta G_1^0,\Delta G_2^0,\Delta G_3^0,\Delta G_4^0)/e - 1.23, \tag{21}$$

where e is the fundamental unit of charge.

In order to evaluate the theoretical potential thermochemically for all four proton–electron transfer steps on the surfaces of the $Au_{13}@Ni_{120}P_{50}$ and the $Ni_{12}P_5(001)$ supported by bulk Au, free energy diagrams were obtained as the first start towards an overall perspective of the reaction path. The free energy diagram for the ideal (*i.e.* virtually nonexistent) $Au_{13}@Ni_{120}P_{50}$ and $Ni_{12}P_5(001)$ catalysts supported by bulk Au are shown in Fig. 4. The ideal catalyst can promote the oxidation of water just above the equilibrium potential in Fig. 4(a). This requires all four proton–electron transfer steps to have the same magnitude (1.23 eV) of reaction free energy at zero potential, which is equal to all the reaction free energy increments being zero at the equilibrium potential of 1.23 V. The nonexistent catalyst that completes this requirement is thermochemically ideal.[53] However, real catalysts do not approach this perfect performance. The calculated free energy diagrams at standard conditions of OER on the surfaces of the $Au_{13}@Ni_{120}P_{50}$ nanocluster and $Ni_{12}P_5(001)$ supported by bulk Au are shown in Fig. 4(b) and (c). It is natural to see that all four elementary steps are uphill at U = 0 V. At standard equilibrium potential (U = 1.23 V), reaction step 1 (ΔG_1^0) and step 4 (ΔG_4^0) go downhill, but others (ΔG_2^0 and ΔG_3^0) still go uphill for $Au_{13}@Ni_{120}P_{50}$, while for the $Ni_{12}P_5(001)$ catalysts supported by bulk Au, reactions step 1 (ΔG_1^0), step 2 (ΔG_2^0) and step 4 (ΔG_4^0) go downhill, but step 3 (ΔG_3^0) remains uphill. The largest free energy shift occurred in step 3 (ΔG_3^0) for both catalysts. Free energy changes (ΔG_{1-4}) of all four elementary reaction steps at standard conditions are summarized in Table 4. We concluded that step 3 (ΔG_3^0) is the potential-determining step for both catalysts because of the largest free energy increment among all four elementary steps. As shown in Table 4, the theoretical overpotential calculated (corresponding to ΔG_3^0) was 0.74 V for the $Au_{13}@Ni_{120}P_{50}$ catalyst,

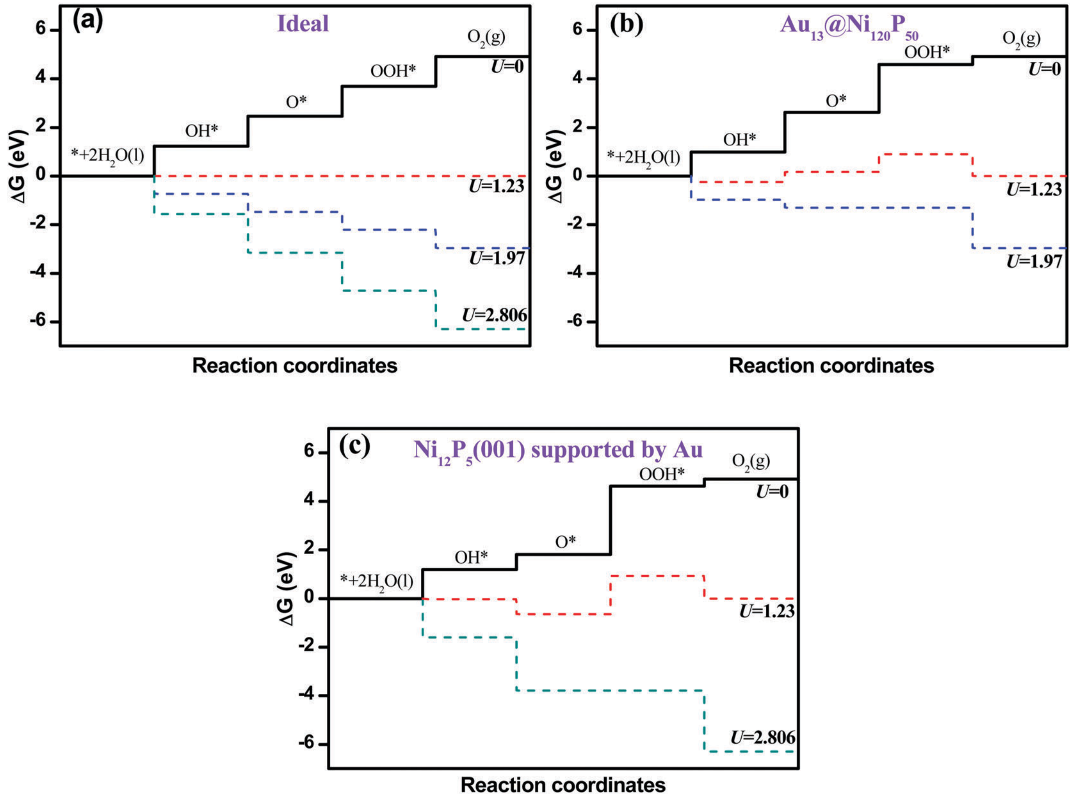

Fig. 4 Free energy diagrams for the OER at zero potential (U = 0 V), equilibrium potential for oxygen evolution (U = 1.23 V), and the potential at which all four elementary steps go just downhill at standard conditions. (a) The ideal catalyst; (b) the $Au_{13}@Ni_{120}P_{50}$ catalyst; (c) the $Ni_{12}P_5(001)$ catalysts supported by bulk Au.

Table 4 Standard free energy change (ΔG_{1-4}) of each proton–electron transfer step at standard conditions (U = 0, pH = 0 and T = 298.15 K) for OER on both $Au_{13}@Ni_{120}P_{50}$ nanocluster and $Ni_{12}P_5(001)$ supported by bulk Au, respectively. Unit of energy is eV

System	ΔG_1^0	ΔG_2^0	ΔG_3^0	ΔG_5^0
$Au_{13}@Ni_{120}P_{50}$	1.641	0.979	1.97	0.33
$Ni_{12}P_5(001)$/bulk Au	1.196	0.61	2.806	0.309

which is actually 0.836 V smaller than that of the $Ni_{12}P_5(001)$ catalysts supported by bulk Au, indicating that the catalytic performance of $Au_{13}@Ni_{120}P_{50}$ is far superior to that of $Ni_{12}P_5(001)$.

3.5 Reaction potential energy surfaces

The thermodynamic discussion presented in the previous section neglected the barriers between the intermediates. In order to comprehensively understand the OER process on the anode in the electrolyzer, detailed potential energy changes along all four consecutive elementary steps are presented in Fig. 5 for both the bumpy $Au_{13}@Ni_{120}P_{50}$ cluster and clean $Ni_{12}P_5(001)$ supported by bulk Au. As shown in Fig. 5, at first, gas water molecules interacted with the bumpy cluster surface and flat $Ni_{12}P_5(001)$ surface, with the adsorption energy of −0.831 eV and −0.802 eV, respectively. Strong adsorption strength on the catalytic surface for molecular H_2O is an important prerequisite for the water-splitting catalytic reaction. For the cluster catalyst, the reactive energy barrier of TS1 is 0.821 eV, 0.1 eV smaller compared to the two free H_2O molecules; for the $Ni_{12}P_5(001)$ supported by bulk Au, the reactive energy barrier of TS1 is 1.346 eV, 0.544 eV larger compared to the two free H_2O molecules (step 1 in Fig. 5), suggesting that H_2O* would rather experience a desorption away from the catalyst surface than decompose into radicals OH* and H*, which is

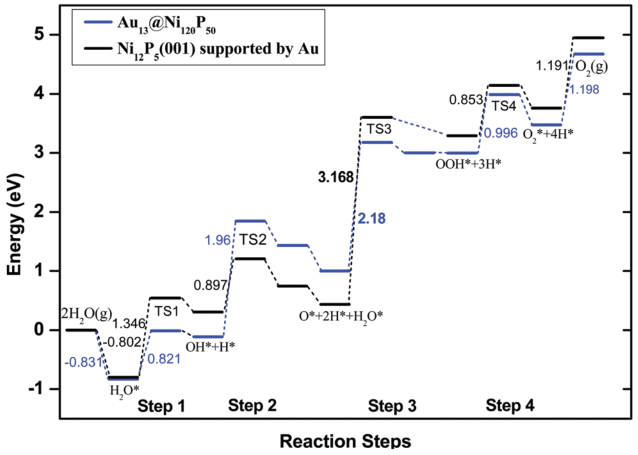

Fig. 5 Potential energy changes of the four consecutive elementary reaction steps for OER on the surfaces of both bumpy $Au_{13}@Ni_{120}P_{50}$ nanocluster (blue bar) and clean $Ni_{12}P_5(001)$ supported by bulk Au (black bar), respectively. The energy reference corresponds to the stable H_2O molecule, core–shell cluster, or clean $Ni_{12}P_5(001)$ slab. The asterisk denotes adsorbed surface sites. Step 1 denotes reaction eqn (4), step 2 eqn (5), step 3 eqn (6), and step 4 eqn (7).

Table 5 Reaction energy (ΔE_{1-4}) and energy barrier (E_{a1-a4}) of all four elementary steps for OER on both $Au_{13}@Ni_{120}P_{50}$ nanocluster and clean $Ni_{12}P_5(001)$ supported by bulk Au. Unit of energy is eV

	Step 1		Step 2		Step 3		Step 4	
System	ΔE_1	E_{a1}	ΔE_2	E_{a2}	ΔE_3	E_{a3}	ΔE_4	E_{a4}
$Au_{13}@Ni_{120}P_{50}$	0.719	0.821	1.547	1.96	2.001	2.18	0.478	0.996
$Ni_{12}P_5(001)$/bulk Au	1.11	1.346	0.442	0.897	2.856	3.168	0.466	0.853

unfavorable for subsequent water-splitting reaction. Analogously, the barrier of O_2* hydrogenation (reverse reaction of Step 4 in Fig. 5) for cluster is 0.68 eV (0.804 eV for $Ni_{12}P_5(001)$; see Table 5) lower than the absolute adsorption energy of O_2 in the O^2 top(Ni_v) configuration, which means that the adsorbed O_2 prefers to hydrogenate than desorb.

For step 1, reactively, the splitting reaction of H_2O* into OH* and H* adsorbates is more competitive on the $Au_{13}@Ni_{120}P_{50}$ nanocluster surface than on $Ni_{12}P_5(001)$ surface according to the energy barrier of 0.821 eV *vs.* 1.346 eV. The elementary reactive step consumes the energy of 0.719 eV for $Au_{13}@Ni_{120}P_{50}$ [1.11 eV for $Ni_{12}P_5(001)$]. Energy barrier (E_{a1}) is less by 0.525 eV for $Au_{13}@Ni_{120}P_{50}$ than $Ni_{12}P_5(001)$, see Table 5.

The previous reaction step is taken as the initial state in step 2. For the final state in step 2, O* adatom is located selectively at the normal site where radical OH* lies in the former step 1, and H atom is adsorbed near the top P atom site. Unlike step 1, the reaction energy and energy barrier for $Au_{13}@Ni_{120}P_{50}$ are larger than for $Ni_{12}P_5(001)$. For the second elementary step reaction on $Au_{13}@Ni_{120}P_{50}$, the energy barrier is 1.96 eV, and the reaction is endothermic by 1.547 eV, while the energy barrier of 0.897 eV and reaction energy of 0.442 eV are found for $Ni_{12}P_5(001)$.

For the third elementary reaction (step 3 in Fig. 5), another H_2O molecule that approaches the catalyst surface moves to an adsorbed O* atom, and finally the configuration has been formed as the current initial state, in which H_2O preferentially stays at the top of the adsorbed oxygen atom. For the final state, we consider that the OH fragment cut from H_2O* binds with O* adatom to form OOH* radical, and new atomic H* is located nearby at the Ni hollow site. This reaction step is the most difficult to proceed because of its highest energy barrier and reaction energy. The reaction step for $Au_{13}@Ni_{120}P_{50}$ needs to overcome the energy barrier of 2.18 eV [3.168 eV for $Ni_{12}P_5(001)$] to get over TS3; comparatively, it proceeds more smoothly for the reaction on the $Au_{13}@Ni_{120}P_{50}$ core–shell cluster than $Ni_{12}P_5(001)$ supported by bulk Au.

For the last step 4 in Fig. 5, the two catalysts have similar performance. It seems to be easier to form O_2* by stripping H from OOH*, whose reaction energy and energy barrier are both easily overcome with applied potential to form O_2 molecule and eventually release off the aqueous solution on the anode side.

The distinct OER performance originates from the differences in adsorption strengths (in Tables 2 and 3) between species and surfaces of the two catalysts. Moderate adsorption in all four consecutive elementary steps is critical for effective OER. In order to illustrate the catalytic performance as the function of adsorption strength, the third elementary reaction (step 3 in Fig. 5) was considered as a representative due to the reaction-determining step in OER. For the initial state of TS3 on $Ni_{12}P_5(001)$ supported by bulk Au, we have calculated and concluded that O* failed to form the stable or metastable configuration with O top(Ni), but preferentially located at the neighboring atomic P top site with the larger adsorption strength of 5.996 eV (absolute value of adsorption energy in Table 3). For $Au_{13}@Ni_{120}P_{50}$, the metastable O top(Ni_v) adsorption configuration was obtained at the smaller binding strength of 4.084 eV (absolute value of adsorption energy in Table 2). Larger interaction (5.996 eV) for radical O* at $Ni_{12}P_5(001)$ supported by bulk Au has given rise to an obstacle to interacting with another free H_2O in aqueous solution to the OOH* radical, while the smaller adsorption strength of 4.084 eV with O top(Ni_v) configuration is favorable for the next reaction (O* + H_2O → OOH* + H*).

The diversity of adsorption strengths may be mostly attributed to differences of the respective specific surfaces exposed in the two model structures. For $Au_{13}@Ni_{120}P_{50}$, the size effect of nanoparticles when binding reaction intermediates (especially for O, OOH species) to active atoms at the surface plays a role in catalytic activity.[54,55] Nanosize-induced contraction increases with decreasing nanoparticle size. The increase of specific surface of active atoms and the reduction of the average bond lengths for exposed facets due to contraction of the core–shell jointly promote catalytic performance compared to that of $Ni_{12}P_5(001)$ supported by bulk Au. Besides, compared with the even surface of $Ni_{12}P_5(001)$, the bumpy core–shell structure allows protruding active Ni atoms to be exposed to a lower surface coordination number[56–58] which strengthens the activity of active atoms.

Moreover, because of structural difference of the amorphous and bumpy $Au_{13}@Ni_{120}P_{50}$ core–shell *versus* the ordered and even $Ni_{12}P_5(001)$ supported by bulk Au, the Au entity has different contributions to the two types of catalysts. Plots of 2D charge density difference are presented for both models.

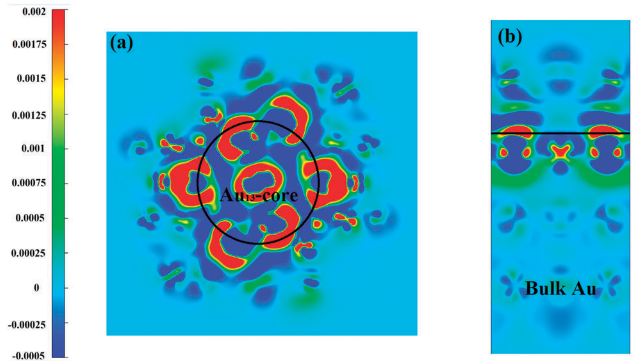

Fig. 6 Plots of the 2D electron density difference. (a) $Au_{13}@Ni_{120}P_{50}$, (b) $Ni_{12}P_5(001)$ supported by bulk Au.

As shown in Fig. 6, the charge density distribution of the Au_{13} core is more diffuse in $Au_{13}@Ni_{120}P_{50}$ than that of bulk Au substrate in $Ni_{12}P_5(001)$ supported by bulk Au, which tunes and appropriately modifies the electronic structure of the exposed surface of $Au_{13}@Ni_{120}P_{50}$ and thus moderates adsorption strength between adsorbed species and catalysts.

For all four consecutive proton–electron transfer steps, we concluded that the third elementary reaction is the rate-limiting step, and as a whole, the performance of $Au_{13}@Ni_{120}P_{50}$ hetero-nanocluster catalyst for OER is far superior than that of $Ni_{12}P_5(001)$ supported by bulk Au (energy barrier of 2.18 eV *vs.* 3.168 eV). Therefore, the study of minimum kinetic reaction energy

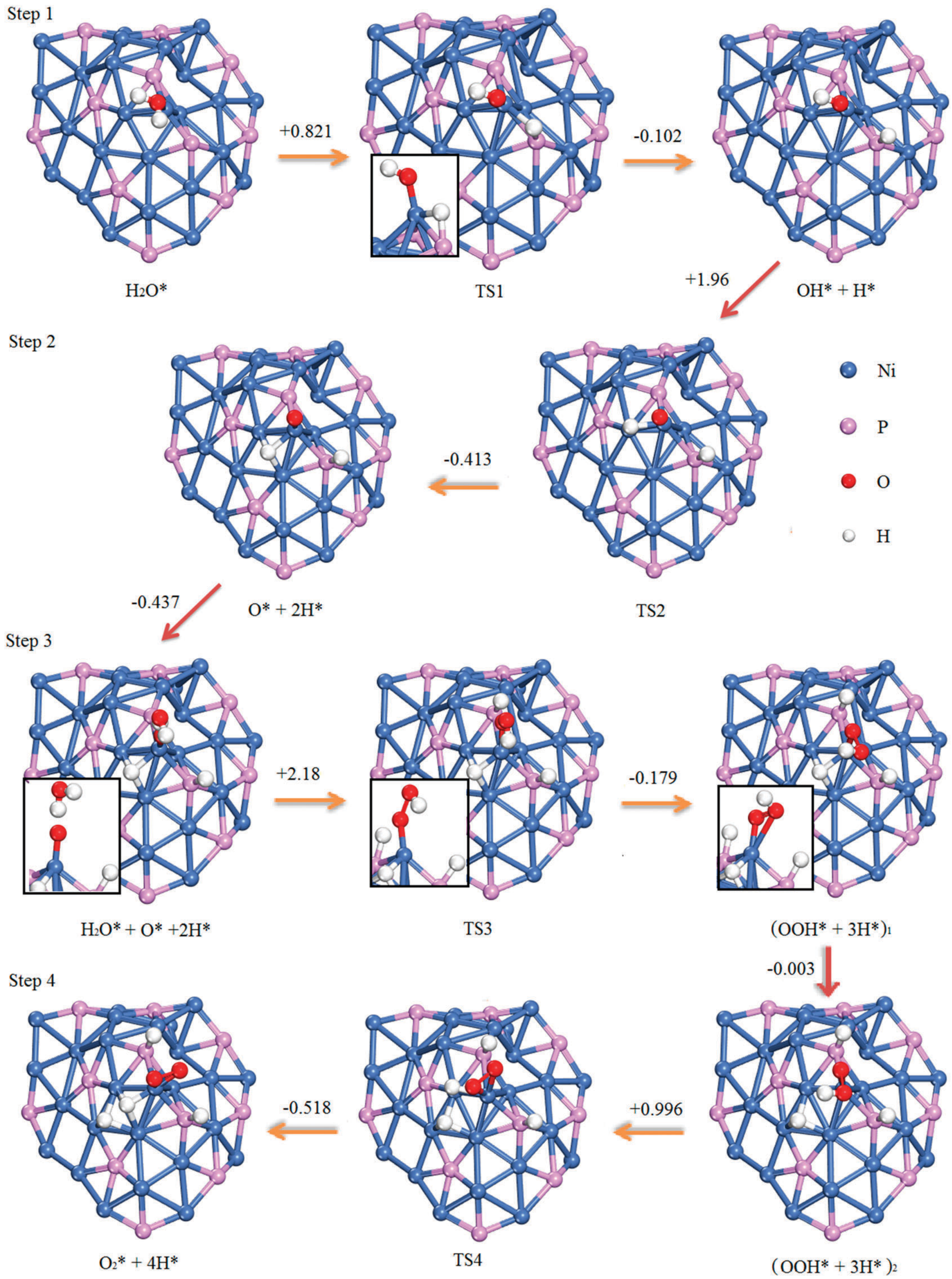

Fig. 7 Minimum kinetic reaction energy pathway along the four consecutive proton–electron transfer steps on the core–shell cluster surface for OER. The number above the arrows is the total energy difference between the former and latter configurations; a positive value denotes an uphill process. The unit of energy is eV.

pathway of OER on only the $Au_{13}@Ni_{120}P_{50}$ catalyst was taken into account in the following section.

3.4 Kinetic reaction pathway

Potential energy changes along four consecutive proton–electron transfer steps were described and discussed above for both $Au_{13}@Ni_{120}P_{50}$ cluster and $Ni_{12}P_5(001)$ surfaces supported by bulk Au. The energy barrier levels between the intermediates indicate that catalytic OER steps proceed more smoothly on the bumpy cluster surface than on flat $Ni_{12}P_5(001)$ surface. In order to carefully clarify the precise OER mechanism, we explore the minimum kinetic reaction energy pathway on the cluster surface in this section (Fig. 7). In the first intermediate step (step 1 in Fig. 7), molecular water is located preferentially at the convex Ni top site through atomic oxygen with the adsorption energy of −0.831 eV, for which weak chemisorption might have occurred. Upon stable adsorption, HOH angle is 106°, stretched by about 2° compared to free water molecule. This indicates that the water molecule has been disturbed more or less by the catalyst presence, which contributes to the catalytic decomposition of water. The first H_2O^* molecule split to OH^* and H^* needs to overcome an energy barrier of 0.821 eV to form OH^*–H^* groups. In other words, a theoretical potential of 0.821 V has to be applied to the electrode to get H_2O^* across the kinetic barrier (transition state TS1) to break down into radical OH^* and H^* adsorbates. The H species dissociated from H_2O^* adsorbed on cluster surface is located momentarily at the top of its nearest neighboring P atom.

OH^* radical remaining on the cluster surface dissociates further to O^* and H^* species under applied potential. In the second intermediate step (step 2 in Fig. 7), the kinetic energy barrier required for OH^* radical to decompose to O^* and H^* species is even larger (1.96 eV) compared with step 1. This may be attributed to the fact that OH^* radical from water splitting binds strongly to the cluster surface with the adsorption energy of −3.392 eV. Such interaction between OH and the cluster surface causes the system to be in a relatively stable state. In step 2, radical H^*, dissociated from the OH^* species, crosses over TS2 with the applied theoretical potential of 1.96 V, where atomic H^* rests momentarily at the Ni–Ni bridge site with bond lengths of 1.656 Å and 1.594 Å, and finally was located firmly at the adjoining Ni hollow site. For the final state of step 2, O^* atom binds directly to the Ni atom that interacted previously with OH, and its binding energy is −4.08 eV.

O^* adsorbate, joined with another H_2O molecule, continued to participate in subsequent reactions (step 3 in Fig. 7). Step 3 is a crucial reaction step due to the start of formation of the O_2 molecule. The second water molecule in aqueous solution moves energetically to the top of atomic O^* adsorbed previously on the cluster surface. By virtue of potential (2.18 V) exerted on the $Au_{13}@Ni_{120}P_{50}$ surface, the water molecule has gained enough active energy from the electrode to overcome a high energy barrier of 2.18 eV (TS3) to form intermediate OOH^*. In this state, radical H is stripped off of the new H_2O molecule and binds to the nearest P atom with the H top(P_v) configuration. New generated intermediate OOH^* radical is located at the normal site with the O^2 bridge(Ni_v^2) configuration. Step 3 is the rate-limiting step, for it experiences the largest kinetic energy barrier in the entire four-step OER process (0.821 eV for TS1, 1.96 eV for TS2, 2.18 eV for TS3 and 0.996 eV for TS4), which is in good agreement with the previous analysis.

As for the last reaction step (step 4 in Fig. 7), it proceeds smoothly and OOH^* continues to dehydrogenate sequentially to generate molecular O_2^* at the small expense of 0.996 eV energy barrier. It was understandable that two oxygen atoms of the OOH^* species both bind to the same atomic Ni from the cluster surface, which weakens the O–H bond strength of radical OOH^*. A new radical H from OOH^* species stayed close at the Ni hollow site. The newly formed molecular O_2^* adsorbs at convex Ni top site, which needs 1.198 eV to desorb from the surface to become a free molecule released in aqueous solution.

4. Conclusions

In summary, the $Au_{13}@Ni_{120}P_{50}$ core–shell nanocluster is a promising catalyst whose structure and precise catalytic mechanism for OER have been investigated based on periodic DFT with D3 correction. We have developed the amorphous $Au_{13}@Ni_{120}P_{50}$ core–shell nanocluster with ∼1.5 nm diameter, and its thermal stability at 300 K is acceptable. As a prerequisite for OER, adsorption structures, adsorption energies and structural parameters of species (H_2O, OH, H, OH, OOH, O_2) involved in OER on both $Au_{13}@Ni_{120}P_{50}$ cluster and $Ni_{12}P_5(001)$ supported by bulk Au are summarized and analyzed.

Moreover, free energy diagrams of the four elementary steps for OER are discussed thermodynamically. The third intermediate reaction (OOH^*) is the potential-determining step. Overpotential of OER for $Au_{13}@Ni_{120}P_{50}$ is 0.74 V, which is 0.836 V smaller than that of $Ni_{12}P_5(001)$ supported by bulk Au. Furthermore, in order to explore comprehensively the OER process, kinetic potential energy changes are studied. The third elementary reaction, as the rate-limiting step, shows the highest reaction energy barrier in all four proton–electron transfer reaction steps, which is in agreement with the thermodynamic results. The kinetic energy barrier is 2.18 eV for $Au_{13}@Ni_{120}P_{50}$ cluster, lower than the 3.168 eV for $Ni_{12}P_5(001)$ supported by bulk Au. The minimum kinetic reaction pathway of oxygen evolution is further exhibited in detail for $Au_{13}@Ni_{120}P_{50}$.

Conflicts of interest

There are no conflicts to declare.

Acknowledgements

The work was supported by the National Key R&D Plan (No. 2016YFB0700500).

References

1 M. Gräetzel, *Acc. Chem. Res.*, 1981, **14**, 376–384.
2 G. W. Crabtree, M. S. Dresselhaus and M. V. Buchanan, *Phys. Today*, 2004, **57**, 39–44.

3 D. G. Nocera, *Acc. Chem. Res.*, 2012, **45**, 767–776.
4 J. A. Turner, *Science*, 1999, **285**, 687–689.
5 M. G. Walter, E. L. Warren, J. R. McKone, S. W. Boettcher, Q. Mi, E. A. Santori and N. S. Lewis, *Chem. Rev.*, 2010, **110**, 6446–6473.
6 S. Lewis and D. G. Nocera, *Proc. Natl. Acad. Sci. U. S. A.*, 2006, **103**, 15729–15735.
7 J. Luo, J. Im, M. T. Mayer, M. Schreier, M. K. Nazeeruddin, N. G. Park, S. D. Tilley, H. Fan and M. Grätzel, *Science*, 2014, **345**, 1593–1596.
8 K. Zeng and D. Zhang, *Prog. Energy Combust. Sci.*, 2010, **36**, 307–326.
9 W. T. Hong, M. Risch, K. A. Stoerzinger, A. Grimaud, J. Suntivich and S. Yang, *Energy Environ. Sci.*, 2015, **8**, 1404–1427.
10 Y. Wang, K. Jiang, H. Zhang, T. Zhou, J. Wang, W. Wei, Z. Yang, X. Sun, W. B. Cai and G. Zheng, *Adv. Sci.*, 2015, **2**, 1500003.
11 M. W. Kanan and D. G. Nocera, *Science*, 2008, **321**, 1072–1075.
12 W. J. Youngblood, S. A. Lee, Y. Kobayashi, E. A. Hernandez-Pagan, P. G. Hoertz, T. A. Moore, A. L. Moore, D. Gust and T. E. Mallouk, *J. Am. Chem. Soc.*, 2009, **131**, 926–927.
13 T. Y. Ma, S. Dai, M. Jaroniec and S. Z. Qiao, *J. Am. Chem. Soc.*, 2014, **136**, 13925–13931.
14 J. Yano, J. Kern, K. Sauer, M. J. Latimer, Y. Pushkar, J. Biesiadka, B. Loll, W. Saenger, J. Messinger, A. Zouni and V. K. Yachandra, *Science*, 2006, **314**, 821–825.
15 S. Chen, J. Duan, M. Jaroniec and S. Z. Qiao, *Angew. Chem., Int. Ed.*, 2013, **52**, 13567–13570.
16 L. Duan, F. Bozoglian, S. Mandal, B. Stewart, T. Privalov, A. Llobet and L. Sun, *Nat. Chem.*, 2012, **4**, 418–423.
17 D. Li, H. Baydoun, C. N. Verani and S. L. Brock, *J. Am. Chem. Soc.*, 2016, **138**, 4006–4009.
18 Y. Lee, J. Suntivich, K. J. May, E. E. Perry and S. Yang, *J. Am. Chem. Soc.*, 2012, **3**, 399–404.
19 T. Takashima, K. Hashimoto and R. Nakamura, *J. Am. Chem. Soc.*, 2012, **134**, 1519–1527.
20 K. L. Pickrahn, S. W. Park, Y. Gorlin, H. Lee, T. F. Jaramillo and S. F. Bent, *Adv. Energy Mater.*, 2012, **2**, 1269–1277.
21 T. L. Wee, B. D. Sherman, D. Gust, A. L. Moore, T. A. Moore, Y. Liu and J. C. Scaiano, *J. Am. Chem. Soc.*, 2011, **133**, 16742–16745.
22 F. Jiao and H. Frei, *Energy Environ. Sci.*, 2010, **3**, 1018–1027.
23 A. J. Esswein, Y. Surendranath, S. Y. Reece and D. G. Nocera, *Energy Environ. Sci.*, 2011, **4**, 499–504.
24 Y. Li, P. Hasin and Y. Wu, *Adv. Mater.*, 2010, **22**, 1926–1929.
25 H. C. Chien, W. Y. Cheng, Y. H. Wang, T. Y. Wei and S. Y. Lu, *J. Mater. Chem.*, 2011, **21**, 18180.
26 J. Suntivich, K. J. May, H. A. Gasteiger, J. B. Goodenough and S. Yang, *Science*, 2011, **334**, 1383–1385.
27 B. B. Cui, H. Lin, J. Li, X. Li, J. Yang and J. Tao, *Adv. Funct. Mater.*, 2008, **18**, 1440–1447.
28 R. N. Singh, D. Mishra, Anindita, A. S. K. Sinha and A. Singh, *Electrochem. Commun.*, 2007, **9**, 1369–1373.
29 Y. Xu, S. Duan, H. Li, M. Yang, S. Wang, X. Wang and R. Wang, *Nano Res.*, 2017, **10**, 3103–3112.
30 L. A. Stern, L. Feng, F. Song and X. Hu, *Energy Environ. Sci.*, 2015, **8**, 2347–2351.
31 A. Han, H. Chen, Z. Sun, J. Xu and P. Du, *Chem. Commun.*, 2015, **51**, 11626–11629.
32 P. Wang, F. Song, R. Amal, Y. H. Ng and X. Hu, *ChemSusChem*, 2016, **9**, 472–477.
33 M. Liu and J. Li, *ACS Appl. Mater. Interfaces*, 2016, **8**, 2158–2165.
34 C. C. Hou, S. Cao, W. F. Fu and Y. Chen, *ACS Appl. Mater. Interfaces*, 2015, **7**, 28412–28419.
35 J. Chang, Y. Xiao, M. Xiao, J. Ge, C. Liu and W. Xing, *ACS Catal.*, 2015, **5**, 6874–6878.
36 M. Adriana, H. Zhu, Y. Yu, Q. Li, L. Zhou, D. Su, M. J. Kramer and S. Sun, *Angew. Chem., Int. Ed.*, 2015, **54**, 9642–9645.
37 M. Adriana, D. Su and S. Sun, *Nanoscale*, 2016, **8**, 3244–3247.
38 S. T. Oyama, *J. Catal.*, 2003, **216**, 343–352.
39 G. Kresse and J. Furthmüller, *Phys. Rev. B: Condens. Matter Mater. Phys.*, 1996, **54**, 11169–11186.
40 J. P. Perdew, K. Burke and M. Ernzerhof, *Phys. Rev. Lett.*, 1996, **77**, 3865–3868.
41 P. E. Blöchl, *Phys. Rev. B: Condens. Matter Mater. Phys.*, 1994, **50**, 17953–17979.
42 S. Grimme, J. Antony, S. Ehrlich and H. Krieg, *J. Chem. Phys.*, 2010, **132**, 154104.
43 J. L. F. Da Silva, C. Stampfl and M. Scheffler, *Phys. Rev. Lett.*, 2003, **90**, 066104.
44 J. L. F. Da Silva, C. Stampfl and M. Scheffler, *Phys. Rev. B: Condens. Matter Mater. Phys.*, 2005, **72**, 075424.
45 G. Henkelman, B. P. Uberuaga and H. Jónsson, *J. Chem. Phys.*, 2000, **113**, 9901–9904.
46 Y. Ni, K. Liao and J. Li, *CrystEngComm*, 2010, **12**, 1568.
47 T. Tsuchiya and K. Kawamura, *J. Chem. Phys.*, 2002, **116**, 2121–2124.
48 D. Fuks, M. V. Landau and M. Herskowitz, *J. Phys. Chem. C*, 2010, **114**, 13313–13321.
49 P. Tereshchuk and J. L. F. Da Silva, *J. Phys. Chem. C*, 2012, **116**, 24695–24705.
50 W. S. Benedict, N. Gailar and E. K. Plyler, *J. Chem. Phys.*, 1956, **24**, 1139–1165.
51 E. Skúlason, V. Tripkovic, M. E. Björketun, S. Gudmundsdóttir, G. Karlberg, J. Rossmeisl, T. Bligaard, H. Jónsson and J. K. Nørskov, *J. Phys. Chem. C*, 2010, **114**, 18182–18197.
52 L. C. Seitz, C. F. Dickens, K. Nishio, Y. Hikita, J. Montoya, A. Doyle, C. Kirk, A. Vojvodic, H. Y. Hwang, J. K. Norskov and T. F. Jaramillo, *Science*, 2016, **353**, 1011–1014.
53 I. C. Man, H. Y. Su, C. Federico, H. A. Hansen, J. I. Martínez, N. G. Inoglu, J. Kitchin, T. F. Jaramillo, J. K. Nørskov and J. Rossmeisl, *ChemCatChem*, 2011, **3**, 1159–1165.
54 X. Wang, H. Inada, L. Wu, Y. Zhu, Y. Choi, P. Liu, W. Zhou and R. R. Aszic, *J. Am. Chem. Soc.*, 2009, **131**, 17298–17302.
55 J. Wu, P. Li, Y. T. Pan, S. Warren, X. Yin and H. Yang, *Chem. Soc. Rev.*, 2012, **41**, 8066–8074.
56 G. Mills, M. S. Gordon and H. Metiu, *J. Chem. Phys.*, 2003, **118**, 4198–4205.
57 A. Ruban, B. Hammer, P. Stoltze, H. L. Skriver and J. K. Nørskov, *J. Mol. Catal. A: Chem.*, 1997, **115**, 421–429.
58 S. N. Rashkeev, A. R. Lupini, S. H. Overbury, S. J. Pennycook and S. T. Pantelides, *Phys. Rev. B: Condens. Matter Mater. Phys.*, 2007, **76**, 035438.